Structural and electronic properties of dual plasma codeposited mixed-phase amorphous/nanocrystalline thin films

Y. Adjallah,[1] C. Anderson,[2] U. Kortshagen,[2] and J. Kakalios[1,a)]
[1]*School of Physics and Astronomy, University of Minnesota, Minneapolis, Minnesota 55455, USA*
[2]*Department of Mechanical Engineering, University of Minnesota, Minneapolis, Minnesota 55455, USA*

(Received 21 November 2009; accepted 7 December 2009; published online 22 February 2010)

A dual-plasma codeposition system capable of synthesizing thin films of mixed-phase materials consisting of nanoparticles of one type of material embedded within a thin film semiconductor or insulator matrix is described. This codeposition process is illustrated by the growth of hydrogenated amorphous silicon (a-Si:H) films containing silicon nanocrystalline inclusions (a/nc-Si:H). A capacitively coupled flow-through plasma reactor is used to generate silicon nanocrystallites of diameter 5 nm, which are entrained by a carrier gas and introduced into a capacitively coupled plasma enhanced chemical vapor deposition reactor with parallel plate electrodes, in which a-Si:H is synthesized. The structural and electronic properties of these mixed-phase a/nc-Si:H films are investigated as a function of the silicon nanocrystal concentration. At a moderate concentration (crystalline fraction 0.02–0.04) of silicon nanocrystallites, the dark conductivity is enhanced by up to several orders of magnitude compared to mixed-phase films with either lower or higher densities of nanoparticle inclusions. These results are interpreted in terms of a model whereby in films with a low nanocrystal concentration, conduction is influenced by charges donated into the a-Si:H film by the inclusions, while at high nanocrystal densities electronic transport is affected by increased disorder introduced by the nanoparticles. © *2010 American Institute of Physics*.
[doi:10.1063/1.3285416]

I. INTRODUCTION

Composite materials that make use of varying length scales, from the nanometer scale to the macroscopic, can exhibit structural and optoelectronic properties not easily realized in homogeneous thin films. Mixed-phase materials consisting of nanocrystallites embedded in an amorphous matrix have found application in such diverse areas as high efficiency solar cells (Si crystals in amorphous Si)[1–3] nonvolatile memory and electron emitters (Si crystals in SiO_2),[4–7] electroluminescent devices (Si crystals in SiN_3),[8] and photonic bandgap materials (SiO_2 in Si).[8,9] Processes to grow these materials range from plasma chemical vapor deposition (CVD) under conditions of nanocrystal formation in the gas phase,[4,9–11] surface nucleation of crystals during plasma CVD,[2,3,12,13] deposition and subsequent annealing of nonstoichiometric material (such as $SiO_{x<2}$) leading to crystal formation via phase segregation,[14,15] and direct plasma deposition in a capacitively coupled plasma (CCP) enhanced chemical vapor deposition (PECVD) system, using high gas pressures and a heavily hydrogen-diluted silane precursor.[2,3,16,17]

There has recently been considerable interest in the properties of hydrogenated amorphous silicon thin films containing silicon nanocrystalline inclusions for photovoltaic applications. It is well known that the electronic proprieties of hydrogenated amorphous silicon (a-Si:H) degrade following light exposure, owing to the photocreation of metastable dangling bond defects [traditionally referred to as the Staebler–Wronski effect (SWE)].[18] These light-induced defects reduce the solar conversion efficiency of a-Si:H based photovoltaic devices, and are seen as a major barrier to amorphous silicon fulfilling its technological potential in thin film solar cell applications. Amorphous silicon thin films containing silicon nanocrystallites (a/nc-Si:H) have been reported to exhibit a resistance to light-induced defect formation.[1] These nanostructured silicon films may be synthesized in a PECVD system operated at elevated gas-chamber silane pressures of at least 1000 mTorr and at high rf power densities, so that particle nucleation within the silane plasma can proceed. This process requires the heavy dilution of the reactive gas with hydrogen, in order to control the size of the particles formed within the plasma. The single-chamber process poses limitations for the production of a/nc-Si:H since (1) the concentration of the crystalline particles in the resulting mixed-phase a/nc-Si:H film are not easily controlled and (2) the gas-chamber conditions necessary for nanoparticle creation are not conducive to growing high quality amorphous material, wherein optimal electronic properties of a-Si:H are typically found in films deposited at lower gas-chamber pressures and rf power levels.

In this paper, we describe a dual-plasma codeposition system where the nanocrystalline particles are synthesized in an upstream flow-through tube reactor and are then injected into a second CCP deposition system in which a-Si:H is grown. This process enables the independent control of the diameter of the nanocrystals, their concentration in the mixed-phase film, and the properties of the surrounding amorphous semiconductor matrix. The structural and electrical properties of a/nc-Si:H films produced by this method are reported.

a)Electronic mail: kakalios@umn.edu.

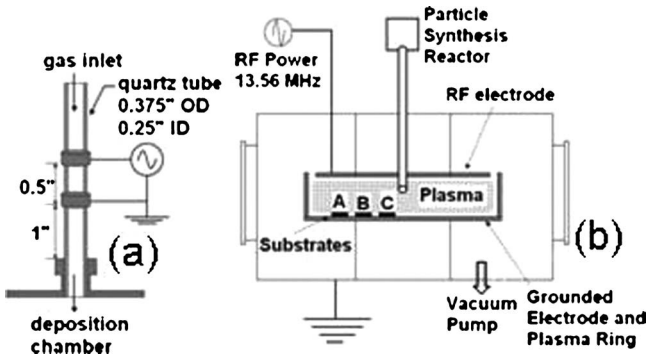

FIG. 1. (a) Nonthermal plasma reactor used to produce Si nanocrystals for codeposited a-Si:H film samples. (b) Sketch of the dual-chamber system that synthesizes mixed-phase a/nc-Si:H thin films. The nanoparticles are grown in the particle synthesis reactor at high pressure, which are then injected into the second chamber. The a/nc-Si:H films are deposited at a lower pressure onto the three glass substrates. The concentration of silicon nanocrystals in the films depends on the substrate position relative to the particle synthesis reactor's injection tube.

II. SAMPLE PREPARATION

A schematic of the plasma reactor used to generate silicon nanocrystals is shown in Fig. 1. The particle synthesis reactor, shown in Fig. 1(a), consists of a 3/8-in.-diameter quartz tube fitted with two ring electrodes.[19] Using an Advanced Energy RFX-600 signal generator/amplifier and a π-type matching network, the excitation voltage at 13.56 MHz was applied to the upper ring electrode in Fig. 1(a), while the lower ring electrode is grounded. By varying the deposition conditions, in particular, the gas-chamber pressure and pulsing the time that the rf plasma is ignited, the diameter of the silicon nanocrystals can be controlled. The gas flow of silane is set at 10 SCCM (SCCM denotes cubic centimeter per minute at STP) of 5% silane prediluted in 95% helium. As a carrier gas to entrain the nanoparticles and deliver them into the second plasma deposition chamber, 50 SCCM of argon was used, for a total pressure of 1.5 Torr. The argon promotes silicon nanocrystal formation. Argon inhibits diffusion losses in the narrow particle synthesis tube, compared to when helium is employed as a carrier gas, enabling the formation of nanocrystallites at lower pressures. Using ~50 W of rf power, a discharge is produced in the tube that extends for a length of around 5 cm, and is extinguished as the tube feeds into the grounded, second deposition chamber [Fig. 1(b)]. The size of the particles is directly related to the gas residence time in the plasma,[19] which was approximately 3 ms under these flow conditions. The average diameter of the particles under the above conditions was between 5 and 6 nm. Transmission electron microscopy (TEM) studies confirm the ability of this reactor to produce small nanocrystals, evidenced by the appearance of lattice fringes in bright-field TEM that are consistent with Si (111) lattice planes.[20] Details of the nanocrystal diameter dependence on chamber gas pressure and plasma residence time have been published previously.[21]

Concurrent with the continuous injection of silicon nanocrystals, a-Si:H is deposited in the lower, CCP chamber, shown in Fig. 1(b). The flow of silane in the second chamber is 20 SCCM of 5% silane in helium, introduced through a separate gas feedthrough from the side of the chamber [not shown in Fig. 1(b)]. Helium is employed for the second deposition chamber, as the lower mass noble gas ion induces less surface damage of the growing thin film semiconductor. The total pressure in the second chamber is 600 mTorr, and the rf (13.56 MHz) power applied across the two electrodes [the rf powered electrode has an area of 315 cm^2 while the grounded electrode (on which the deposition substrates reside) has an area of 1338 cm^2, with a fixed separation of 5 cm] is 5 W. For the films described here the grounded electrode, upon which the substrates reside, is kept at 250 °C while the top rf electrode is unheated.

One method by which the concentration of silicon nanocrystals in the a-Si:H matrix film can be varied is via convection of the argon carrier gas in which the particles from the particle synthesis reactor are entrained.[19] The quartz tube providing the nanoparticle aerosol is fed into the CCP chamber to within a distance of 2.5 cm from the grounded electrode surface. The gas flow from the particle synthesis reactor impinges on the grounded electrode and the flow diverges toward the electrode periphery. Substrates are placed radially outward from the center position of the tube exit, labeled alphabetically from the electrode periphery inward, as shown in Fig. 1(b). The substrate labeled A is located 5 cm horizontally from the quartz tube injection tube, while the substrate labeled B is a distance of 2.5 cm from the particle injection tube, and the substrate labeled C is directly underneath the quartz tube opening. This reactor geometry takes advantage of the fact that the nanoparticles are transported to the substrate surface by diffusion from the gas phase, and that the deposition rate of particles decreases radially outward from the center position of the electrode. We thus have a unique way of studying the effect of crystalline fraction on the film properties. As the lower grounded electrode, on which the substrates reside, is the heated electrode, a positive temperature gradient between the CCP electrodes creates a thermophoretic force directed away from the substrates.[22] The film is deposited onto Corning 7059 glass or crystalline silicon substrates. The film thickness, measured by a profilometer, varies from 200 to 700 nm for plasma deposition times of 60 min with a deposition rate of ~1–2 Å/s. Additional effort is needed to increase these deposition rates for large scale manufacturing applications. The film deposited near the particle tube (location C) is always the thickest (around 700 nm) while the film deposited at 5 cm away (location A) from the particle tube is thinnest, with a film thickness of approximately 200 nm.

Confirmation that the nanoparticle concentration in the a/nc-Si:H films is sensitive to the substrate position relative to the nanocrystal injection tube is provided by measurements of the particle deposition rates, determined by tapping-mode atomic force microscopy (tm-AFM).[19] Figure 2 shows the tm-AFM images for particles deposited for 1 min under plasma conditions similar to the film growth conditions, with the exception that the SiH_4/He feed gas is replaced by pure He, so that no surrounding a-Si:H film is deposited. In this way, all effects of temperature, gas drag, and particle charging were reproduced. The observed area density of particles was the lowest in the periphery region of the electrode [the

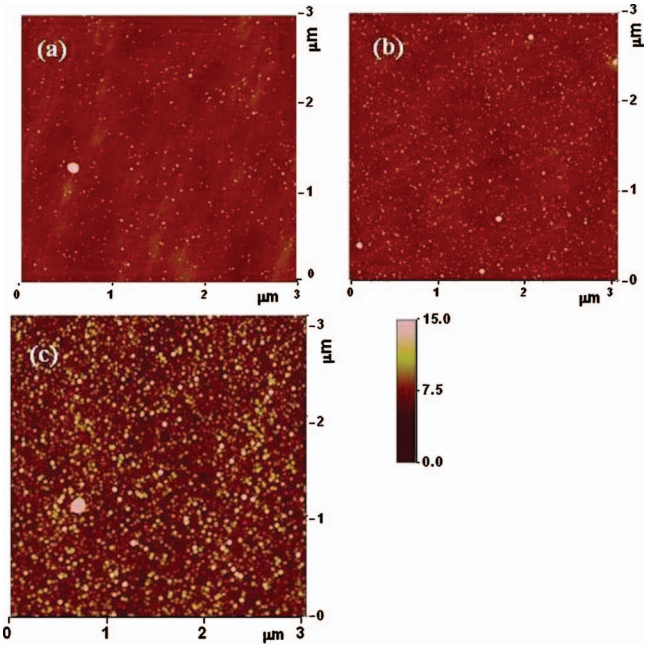

FIG. 2. (Color) AFM images of nanoparticles deposited under typical plasma conditions for 1 min onto c-Si substrates located (a) 5 cm, (b) 2.5 cm, and (c) 0 cm from the electrode center.

substrate position labeled A in Fig. 1(b)], around 80 μm^{-2} at 5 cm. The density increased to 120 μm^{-2} at 2.5 cm, for the substrate labeled B in Fig. 1(b). These particle density values are the average of several measurements across the surface of each substrate. The difference in particle deposition rate is apparently not linear with electrode distance, as the center sample [Fig. 2(c)], labeled substrate C in Fig. 1(b), appears to contain up to 1 ML (monolayer) of particles. Based on the samples at the outer electrode locations [Figs. 2(a) and 2(b)], a slightly lower particle density would have been expected. This suggests that deposition by direct impaction may also play a role for films deposited near the electrode center. The larger features seen in the tm-AFM images could likely be due to particle agglomerates that formed in the gas phase upon leaving the synthesis plasma.

III. EXPERIMENTAL METHODS

The presence and concentration of silicon nanocrystals in the mixed-phase thin films synthesized in the dual-chamber codeposition system are confirmed by measurements of the Raman spectrum. Raman spectra are recorded with a Witec Alpha 300 R confocal Raman microscope equipped with an UHTS 200 spectrometer using an argon ion excitation laser of wavelength 514.4 nm at a power of 5 mW focused to an area of 700 nm diameter. The depth of field of the confocal microscope is approximately 500 nm, comparable to or larger than the thickness of the films being measured. By varying the depth of field for thicker films, we have confirmed that the observed nanocrystalline signal is characteristic of the bulk of the film. The Raman spectra presented are taken using a low incident laser power to avoid any shifts of the peak due to thermal annealing of the sample. Raman spectra are recorded from several different

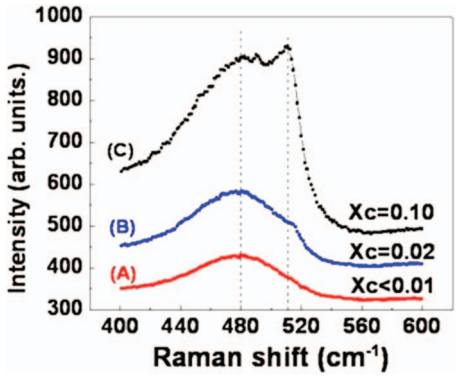

FIG. 3. (Color) Raman absorption spectrum of a/nc-Si:H films as a function of nanocrystalline concentration for run 1 as listed in Table I. The curves are offset vertically for clarity.

locations along the film surface, to ensure that the results are characteristic of the material and do not reflect a local fluctuation in nanocrystal concentration.

The crystalline fraction is the percent, by volume, of the mixed-phase film that is crystalline silicon and can be defined as the ratio of the area under the crystalline silicon peak over the sum of the area under the crystalline silicon peak and the area of the amorphous silicon peak,

$$X_c = (A_{nc})/[A_{nc} + \lambda A_{am}].$$

Comparing the area under the crystalline silicon peak located at 512 cm^{-1} (and at 500 cm^{-1} for the film with the highest nanocrystalline concentration) to the area of the amorphous silicon matrix peak at 480 cm^{-1} and assuming a ratio of the Raman backscattering cross section of the crystalline and the amorphous phase of $\lambda = 1.0$, the films presented in the Fig. 3 (labeled run 1 in Table I) have a crystalline fraction X_c equal to 0.10, 0.02. and less than 0.01 for the mixed-phase films grown at the positions C, B, and A, respectively. The ratio of the Raman backscattering cross-section factor λ is determined from comparisons of Raman spectra for bulk crystalline silicon to pure a-Si:H films, values frequently cited in the literature range from $\lambda = 0.8$ to $\lambda = 0.88$.[23–25] When we use a cross-section factor λ of 0.8–0.88, the calculated X_c increases by a small amount. As we are interested in comparing the effects of a relative increase in nanocrystal concentration, and given that the role that quantum confinement plays on the Raman backscattering cross section is not well understood, we have made the simplifying assumption of $\lambda = 1.0$ for our Raman data.

The nature of the Si–H bonding is another important feature of the codeposited films. A common figure of merit regarding film quality is taken from the relative amounts of clustered H and isolated Si–H bonds, measured by the vibrational bond-stretching modes with either IR absorption[26,27] or Raman spectroscopy.[28] The microstructure fraction R is calculated as

$$R = I_{2090}/(I_{2090} + I_{2000}),$$

where I_{2090} and I_{2000} are the integrated intensities of the peaks centered at the respective wavenumber value. The peak centered at around 2000 cm^{-1} is attributed to the excitation of vibrational modes of isolated Si–H bonds in the

TABLE I. Electronic properties of six deposition runs of mixed-phase a/nc-Si:H, listing the crystalline concentration as determined from Raman measurements, the dark conductivity at 320 K and the activation energy in state A measured near 320 K, the ratio of state B to state A dark conductivity (the SWE), and the photosensitivity, defined as the ratio of the photoconductivity to state A dark conductivity.

Run	Sample position	X_c fraction	E_a, state A (eV)	$\sigma_{d(A)}$ at 320 K (Ω^{-1} cm^{-1})	$\sigma_{d(B)}$ at 320 K (Ω^{-1} cm^{-1})	$\sigma_d(B)/\sigma_d(A)$ at 320 K	σ_{ph} at 320 K (Ω^{-1} cm^{-1})	$\sigma_{ph}/\sigma_d(A)$ at 320 K
1	A	<0.01	0.89	8.30×10^{-12}	8.33×10^{-12}	1.00	6.23×10^{-07}	75 000
	B	0.02	0.82	8.29×10^{-09}	9.73×10^{-09}	1.17	3.19×10^{-05}	3 800
	C	0.1	0.98	8.33×10^{-11}	2.08×10^{-10}	2.50	1.46×10^{-08}	180
2	A	<0.01	0.90	8.33×10^{-12}	8.33×10^{-12}	1.00	7.13×10^{-08}	8 600
	B	0.01	0.64	2.00×10^{-08}	2.57×10^{-09}	0.13	1.73×10^{-04}	8 700
	C	0.18	0.91	1.33×10^{-11}	2.50×10^{-11}	1.88	6.43×10^{-10}	50
3	A	0.02	0.86	1.61×10^{-09}	5.00×10^{-10}	0.31	1.25×10^{-05}	7 800
	B	0.03	0.85	3.72×10^{-09}	3.05×10^{-09}	0.82	2.39×10^{-05}	6 400
	C	0.09	0.96	4.90×10^{-10}	5.08×10^{-10}	1.04	5.45×10^{-07}	1 100
4	A	0.02	0.73	1.79×10^{-09}	1.36×10^{-09}	0.76	4.47×10^{-06}	2 500
	B	0.03	0.80	4.8×10^{-10}	6.92×10^{-10}	1.41	7.15×10^{-07}	1 500
	C	0.19	0.70	3.67×10^{-11}	1.75×10^{-10}	4.77	3.88×10^{-09}	100
5	A	<0.01	0.82	5.83×10^{-10}	1.75×10^{-10}	0.30	2.83×10^{-05}	49 000
	B	<0.01	0.81	2.42×10^{-09}	1.47×10^{-09}	0.61	8.38×10^{-05}	35 000
	C	0.16	0.89	5.00×10^{-11}	4.42×10^{-10}	8.83	6.81×10^{-09}	140
6	A	<0.01	0.92	2.50×10^{-11}	8.33×10^{-12}	0.33	4.67×10^{-07}	19 000
	B	0.04	0.71	2.04×10^{-08}	6.95×10^{-08}	3.40	9.93×10^{-05}	4 900
	C	0.1	0.97	1.37×10^{-09}	2.71×10^{-09}	1.98	2.74×10^{-07}	200

film.[26] The absorption peak around 2090 cm^{-1} can come from several Si–H configurations, including clustered Si–H_x bonds in a-Si:H,[26,27] as well as surface hydrogen modes found in crystalline Si,[26] and is typically associated with higher amounts of structural and electronic disorder.[26,27,29] The infrared absorption spectra for the mixed-phase a/nc-Si:H films deposited onto crystalline silicon substrate are collected with a Nicolet Magna 750 Fourier Transform Infra-Red (FTIR) spectrometer.

For measurements of the electronic transport properties of the mixed-phase films, two coplanar chromium electrodes typically 1 cm long and separated by a gap either 2 or 4 mm wide are evaporated onto the films, which yield linear current-voltage characteristics. The samples are placed in a vacuum chamber and annealed at 450 K for 120 min, in order to remove any influence of light-induced defects or surface adsorbates. The films are then slowly cooled (cooling rate ~1 K/min) to room temperature, where the annealed state (state A) dark conductivity is then measured upon warming (heating rate ~1 K/min) back up to 450 K. Upon returning to room temperature, the sample is then reheated to 320 K, and the photocurrent is measured during a 2 h exposure to white light from a W–Ha heat-filtered white light. This light soaked state is termed state B. The temperature dependence of the dark conductivity of the a/nc-Si:H films are then measured in state B, under the same conditions as before.

IV. STRUCTURAL CHARACTERIZATION

In an earlier preliminary report,[21] we have described TEM studies that verify that silicon nanocrystals are indeed introduced into the amorphous silicon matrix in this codeposition system, and moreover that these crystallites are produced in the particle synthesis reactor, rather than formed within the silane plasma in the CCP chamber. As ion milling can affect the structure of the films, a small angle cleaving technique[30] (SACT) was employed to obtain the cross-section views of these samples. The particle size distribution and the particle crystallinity were analyzed by high-resolution TEM, confirming that the nanocrystallites are present throughout the thickness of the a/nc-Si:H films. Focal series imaging demonstrate that the lattices fringes are not microscope artifacts.[30]

While high-resolution TEM provides direct evidence of nanocrystalline inclusions, it is not particularly useful for quantifying the crystalline content. This is due to the fact that only particles with lattice planes that are properly aligned with respect to the electron beam can be observed directly in TEM. In Fig. 3, we compare the Raman spectra of the a/nc-Si:H films (run 1 from Table I) from the three different positions of the CCP chamber [Fig. 1(b)], corresponding to low, intermediate and high nanocrystalline concentrations as indicated by the tm-AFM observations. The curves are offset to fit onto a single plot.

The a/nc-Si:H film deposited in position A in Fig. 1(b) has a Raman spectrum with a broad peak at a wavelength shift of 480 cm^{-1} corresponding to the TO mode of a-Si:H. A similar broad peak at 480 cm^{-1} is the only peak observed in the Raman spectra in the corresponding wavenumber regime of homogeneous a-Si:H films deposited in the same system with the particle synthesis reactor turned off. This is expected since the deposition rate of nanoparticles (inferred

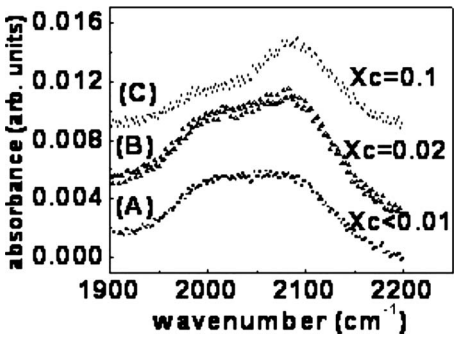

FIG. 4. Infrared absorption spectra of the mixed-phase films as function of crystalline concentration for run 2 as listed in Table I. The curves are offset vertically for clarity.

from the tm-AFM measurements) suggests that a crystalline fraction (defined below) much less than 0.01 would be found. We see that the mixed-phase film deposited in position B [Fig. 1(b)], with intermediate nanocrystallite concentration, has two peaks: one corresponding to the TO mode of a-Si:H at 480 cm^{-1} and the other small crystalline peak at 512 cm^{-1}. The laser power was varied to ensure that this peak location was not due to a temperature shift. The film deposited in the position C in Fig. 1(b) (highest nanocrystallite concentration) has the same two peaks but an enhanced intensity of the 512 cm^{-1} peak and third peak near 500 cm^{-1}.

Bulk crystalline silicon has a sharp peak in the Raman spectrum centered at 518–520 cm^{-1}. The position of the peak can shift to lower wavenumbers due to quantum confinement effects.[23] A peak at 512 cm^{-1}, equivalent to a downward shift of approximately 6 cm^{-1}, is consistent with a nanocrystalline size of ~4 nm (Refs. 23 and 24) in diameter, while the TEM analysis indicates a diameter around 5–6 nm.[21] We also see in the high nanocrystallite concentration samples another small peak at around 500 cm^{-1}, which has been attributed to the grain boundary region surrounding the nanocrystals.[25]

Assuming a crystallite diameter of 5–6 nm and a crystalline fraction of 0.10 for the film with higher nanocrystallite concentration, the nanocrystallites in the film deposited at position C have an average spacing of ~13 nm, while the nanoparticles in the film with the lowest crystalline fraction have an average separation >40 nm. Again it is noted that the trend in the crystalline fraction is not linear with electrode distance, similar to the AFM deposition rate measurements in Fig. 2. Even so, this deposition technique demonstrates a procedure for the inclusion of nanocrystals into amorphous films, with some level of control over their number density. This is a significant contribution toward the understanding of mixed-phase films.

Figure 4 shows the infrared spectra in the range 1900–2200 cm^{-1} for the films from run 2 in Table I,[31] deposited in the A, B, and C positions as indicated in Fig. 1(b); the curves are normalized and offset vertically for clarity. The FTIR spectra can be fitted using two peaks, one at 2000 cm^{-1} and the other at 2090 cm^{-1}. There is a clear increase in infrared absorption at 2090 cm^{-1} as the nanocrystalline concentration in the a/nc-Si:H films increases.

The infrared absorption spectra in Fig. 4 are consistent with an increase in $Si-H_x$ bonding in the grain boundary region surrounding the nanocrystalline inclusions. For samples located far from the electrode center, the Si–H spectra was identical to that observed for pure a-Si:H, where no particles were injected into the plasma, showing a microstructure fraction around $R=0.55$; the additional $Si-H_x$ bonds for the sample at 5 cm from the particle injection tube [labeled sample A in Fig. 1(b)] associated with the nanocrystal surfaces were too few to be detected. As the particle concentration increases for films deposited closer to the particle injection tube, R also increased, up to $R=0.6$ with a corresponding crystallinity of $X_C=0.17$ for the center sample deposited closest to the particle injection tube. Coupled with the fact that the value of R with no particles injected showed no dependence on substrate location, these data support the interpretation that the additional signal from clustered $Si-H_x$ at 2090 cm^{-1} comes from the H atoms at the grain boundaries of the embedded particles.

The deposition of mixed-phase films as in Figs. 3 and 4 have been repeated several times. There is a run to run variation in the exact concentration of silicon nanocrystals embedded within the a-Si:H matrix, even when the deposition conditions under which the mixed-phase a/nc-Si:H films are grown are nominally unchanged. For one particular deposition run, there was essentially no change in the microstructure factor for the films synthesized at positions A and B as in Fig. 1(b), but for the film grown directly underneath the particle injection tube the microstructure factor was nearly 0.9. The general trend is an increase in the silicon nanocrystal concentration, accompanied by an increase in the infrared microstructure factor R, with the largest change in R generally found for films with the highest nanocrystal density.

V. ELECTRONIC CHARACTERIZATION

The structural studies described above confirm that we can generate silicon nanocrystals in one plasma chamber that can be homogeneously incorporated into a hydrogenated amorphous silicon matrix synthesized in another plasma deposition reactor. Moreover, we have a unique platform to investigate the influence of increasing the nanocrystalline inclusion concentration on the optical and electronic properties of mixed-phase a/nc-Si:H films, as the codeposition system enables the simultaneous synthesis of a-Si:H with a varying density of nanoparticle inclusions (Figs. 2 and 3). The surrounding a-Si:H tissue is the same for films deposited in a single run, and the nature of the nanocrystals generated in the particle synthesis chamber [Fig. 1(a)] is unchanged during the deposition. Consequently, the only difference for the a/nc-Si:H films grown at positions A, B, and C in Fig. 1(b) is the density of nanocrystals embedded within the films. The nonlinear sensitivity to nanoparticle concentration of the optical absorption spectra and temperature dependence of the dark conductivity, described below, is consequently not likely to be due to any variations in the quality of the surrounding a-Si:H.

The temperature dependence of the dark conductivity in state A is well described by the Arrhenius function σ

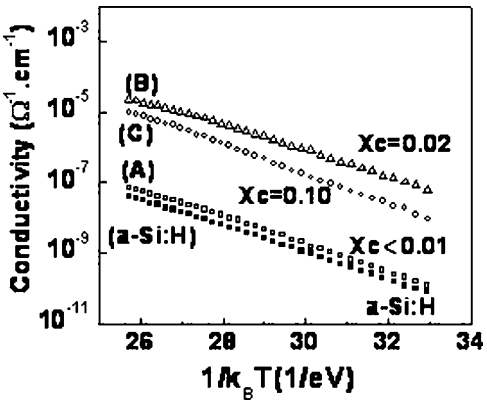

FIG. 5. Arrhenius plot of the dark conductivity of a series of a/nc-Si:H mixed-phase films for run 1 as listed in Table I, with low ($X_C<0.01$), medium ($X_C=0.02$), and high ($X_C=0.10$) crystal fractions. For comparison, the conductivity of a pure a-Si:H film without nanocrystalline inclusions is also plotted.

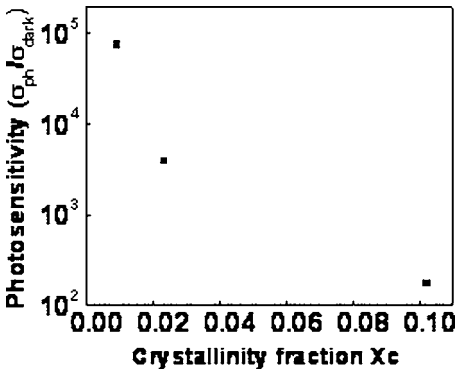

FIG. 6. Plot of the photosensitivity, defined as the ratio of the initial white light photoconductivity to the dark conductivity at 320 K in annealed state A against crystalline fraction as determined for run 1 as listed in Table I of mixed-phase a/nc-Si:H films.

$=\sigma_0 \exp[-E_A/k_BT]$, where E_A is the activation energy and σ_0 is the conductivity prefactor, as shown in Fig. 5 for the same series of films as in Fig. 3. This figure shows the Arrhenius plots for films from a single deposition run (run 1 from Table I) with increasing nanocrystalline concentration, along with an a-Si:H film deposited in a separate run with no nanocrystals included, for reference. The corresponding crystalline fractions are indicated on the plot. For the a/nc-Si:H film with $X_C<0.01$, the electrical behavior is very similar to that of a-Si:H films deposited without embedded nanocrystals, with a room temperature dark conductivity $\sigma \sim 10^{-10}\ \Omega^{-1}\ cm^{-1}$ and an activation energy $E_A=0.89$ eV. The activation energy is fitted to the temperature dependence of the dark conductivity near room temperature. There is a slight downward kink at higher temperatures evident above 430 K for some of the mixed-phase films investigated, which is a hallmark of thermal equilibration effects in undoped a-Si:H. As the crystalline fraction is increased to 0.02, the conductivity increases by several orders of magnitude, along with a reduction in the dark conductivity activation energy to $E_A=0.82$ eV. This trend does not continue with increasing crystalline fraction, as the conductivity for $X_C=0.10$ is intermediate to samples between 0 and 0.02 over the range of temperatures investigated, with a measured activation energy of $E_A=0.91$ eV.

The results from Fig. 4 are unanticipated. In order to confirm that the dark conductivity is indeed nonmonotonic with nanocrystalline concentration, this deposition run was repeated five more times. These data are summarized in Table I, which lists the six runs (the data in Fig. 5 are for run 1), the nanocrystalline concentration as determined by Raman spectra as in Fig. 3, the dark conductivity at 320 K and the activation energy in state A measured near 320 K, the ratio of state B to state A dark conductivity (the SWE), and the photosensitivity, defined as the ratio of the photoconductivity to the state A dark conductivity.

Depositions of mixed-phase films have been repeated several times. In all trials, the general behavior of an enhancement of the dark conductivity, with a decrease in the measured activation energy for the a/nc-Si:H film containing a crystalline fraction of $X_C \sim 0.02-0.04$, as determined by Raman spectroscopy measurements, was observed.

There is a run to run variation in the exact concentration of silicon nanocrystals embedded within the a-Si:H matrix, even when the deposition conditions under which the mixed-phase a/nc-Si:H films are nominally unchanged. The codeposition system shown in Fig. 1 always yields a higher nanocrystalline concentration in the films directly underneath the particle injection tube (location C) than for the films grown at locations A and B. For certain deposition runs, the dark conductivity of the a/nc-Si:H film with the highest nanocrystal concentration was closer to that of the material with the lowest density of nanocrystals. There is scatter in the precise conductivity and activation energies observed between differing runs, for films deposited under nominally identical conditions. The gas convection in the second chamber, employed to vary the concentration of nanocrystals supplied to the different substrates, can lead to variations in the precise concentration of nanocrystals in the mixed-phase films, as determined by Raman spectroscopy measurements. Despite run-to-run variations, in all cases the dark conductivity followed the trend exhibited in Fig. 5.

The initial motivation for investigating mixed-phase a/nc-Si:H films was reports that these materials exhibited improved resistance to light-induced defect formation (the SWE). In order to investigate these materials' sensitivity to light-induced defect creation, the films in Table I were exposed at 320 K to heat-filtered white light from a W–Ha lamp for 2 h. The temperature dependence of the dark conductivity is then remeasured, and the light soaked condition is labeled state B. The ratio of the state B to state A dark conductivity at 320 K, listed in Table I, is observed to be close to unity for a/nc-Si:H films with an increasing concentration of embedded nanocrystals, while films with lower concentrations of nanocrystals displayed a reduction in the dark conductivity due to the SWE of nearly an order of magnitude.

A plot of the photosensitivity, defined as the ratio of the photoconductivity initially recorded to state A dark conductivity at 320 K against crystalline silicon fraction for the same a/nc-Si:H films as in Fig. 5, is shown in Fig. 6. Comparable data are observed for all of the a/nc-Si:H mixed-

phase thin films, as listed in Table I. The decrease in the photosensitivity with increasing nanocrystalline concentration for the films shown in Fig. 6 suggests that these films contain a higher density of recombination centers, most likely midgap dangling bond defects. These dangling bond defects may possibly be associated with the inclusion of the nanoparticles during film growth.

VI. DISCUSSION

By varying the substrate position relative to the particle injection tube in the second reactor chamber where the a-Si:H is deposited, a series of films can be grown in a single deposition run in the dual-chamber codeposition system, where the nanoparticle concentration varies from $X_c < 0.01$ to over $X_c = 0.10$ crystalline fraction, as determined by Raman spectroscopy and tm-AFM. We now discuss how this variation in nanocrystal density can account for the electronic properties described above. We begin with a consideration of the structural characteristics of the films.

The Raman peak attributed to the silicon nanocrystals in Fig. 3 is shifted to a wavenumber of approximately 512 cm^{-1}, while bulk crystalline silicon exhibits a TO Raman peak at 518–520 cm^{-1}. Various studies have demonstrated, by growing bulk films comprised solely of silicon nanocrystals (that is, with no surrounding amorphous silicon matrix), that there is a pronounced shift in the Raman TO peak to lower wavenumbers when the diameter of the nanocrystalline particles is less than 10 nm, owing to quantum confinement effects.[23–25] From the data of Viera *et al.*,[23] the shift of approximately 6–8 cm^{-1} observed here would indicate that the nanocrystals in these mixed-phase films have a diameter of approximately 3–4 nm, smaller than the 5–6 nm expected for the deposition parameters employed in the particle synthesis reactor.

Measurements of the infrared absorption spectra, as shown in Fig. 4, find an increase in absorption at 2090 cm^{-1} in films with the highest nanoparticle density. Films deposited when the particle synthesis reactor is off show no variation in the 2090 cm^{-1} absorption intensity with substrate position in the second plasma chamber. These results suggest that the region surrounding the nanocrystals is heavily hydrogenated.[32,33] Unlike the investigations of Viera *et al.*,[23] the nanoparticles in our system must traverse a silane plasma before reaching the deposition substrate, and only then are incorporated into the growing amorphous silicon film, which, at the deposition temperature of 250 °C employed, entails significant hydrogen diffusion and structural relaxation. Elucidation of the role that the specific deposition conditions play on the observed shift in the Raman crystalline TO mode requires additional systematic investigation.

The presence of a hydrogen rich shell surrounding the silicon nanocrystalline inclusions may also play a role in the enhancement of the dark conductivity observed in a/nc-Si:H films having crystalline fractions of a few percent, as explained below. Moreover, if a large proportion of the bonded hydrogen in these mixed-phase films does indeed reside in the shells surrounding the nanocrystalline inclusions, then this could account for the reduced light-induced conductance degradation presented in Table I.

There is no single, generally accepted mechanism underlying metastable defect formation. One popular model posits that the SWE involves the breaking of strained Si–Si bonds due to the nonradiative recombination of photoexcited electron-hole pairs.[34–36] These broken bonds are stabilized by the insertion of hydrogen, forming at least one Si–H bond with the newly created silicon dangling bond states. Alternatively hole trapping could weaken a Si–Si bond, such that subsequent recombination with an electron or hydrogen insertion from diffusion hydrogen atoms could result in metastable defect formation.

In most models for the SWE, the motion of bonded hydrogen plays a central role in either the creation or stabilization of the newly created dangling bond states. If the majority of bonded hydrogen is in the region immediately surrounding the nanocrystalline inclusions, then if bond breaking takes place in the surrounding amorphous silicon matrix, there is less chance for a nearby hydrogen atom to participate in metastable defect formation. In this case the two broken Si bonds are likely to reform, inhibiting metastable defects from being added to the material following illumination. This argument is similar to one put forward to account for the enhanced stability against light-induced defect creation in a-Si:H synthesized using the hot wire technique.[37,38] In these materials the hydrogen content is much lower than in glow discharge deposited material. Nuclear magnetic resonance studies indicate that nearly all the bonded hydrogen in the hot wire a-Si:H resides in clusters of hydrogen, such as in the inner surface of a divacancy, and there is a low concentration of hydrogen in the bulk of the semiconducting material.[39]

We suggest that in the mixed-phase films, the bonded hydrogen predominately (though not exclusively) resides in the region surrounding the nanocrystalline inclusions. A nanocrystal with a diameter of 5 nm contains roughly 3300 silicon atoms, and for a film with an $X_c = 0.1$, this implies a nanocrystal density of 1.5×10^{18} nc/cm^3. If we assume that the "grain boundary" region extends about 0.25 nm from the surface of the nanocrystallite, then each grain boundary volume can accommodate about 1000 atoms, of which potentially half could be hydrogen atoms. This would correspond to a bonded hydrogen density within the shells surrounding the nanocrystals on the order of 1.5 at. %. High electronic quality PECVD a-Si:H typically has a bonded hydrogen content of 8–10 at. %, while films deposited under nonoptimal conditions have higher hydrogen concentrations. The above is only meant as a rough order of magnitude estimate indicating that there appears to be sufficient space in the grain boundary region surrounding each nanocrystalline inclusion to accommodate a significant fraction of the bonded hydrogen in the mixed-phase material.

A possible energy band diagram for the a-Si:H in the vicinity of a silicon nanocrystalline inclusion with an overhydrogenated silicon shell is illustrated by the sketch in Fig. 7. If the silicon cores of the nanocrystals embedded in the a/nc-Si:H do indeed have an average diameter of ~5 nm,

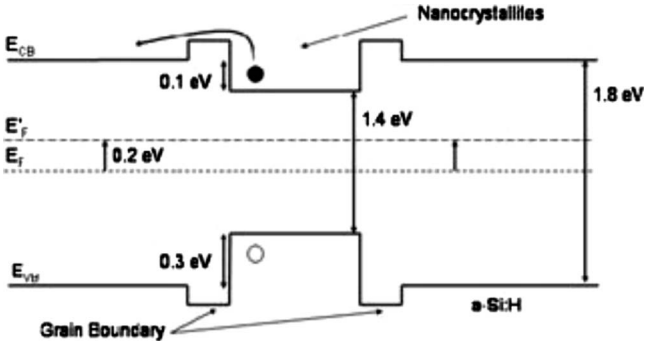

FIG. 7. Sketch of the energy band diagram proposed for a silicon nanocrystal, surrounded by an a-Si–H_x rich shell within an a-Si:H matrix. A thermally excited electron (filled circle) in the nanoparticle can easily overcome the 0.2 eV barrier and can be donated to the a-Si:H film, while the corresponding hole (denoted by an open circle) in the silicon nanocrystal cannot overcome the larger barrier to be injected into the a-Si:H valence band.

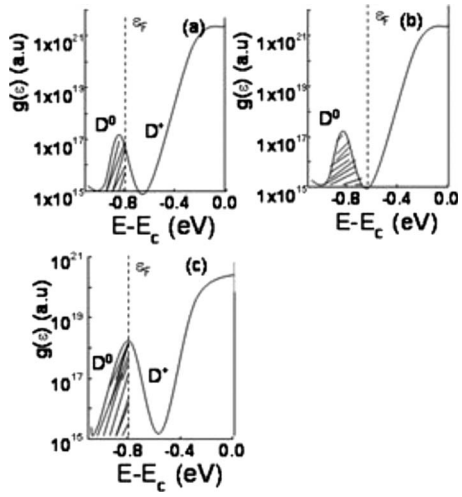

FIG. 8. Sketch of the density of states in the upper half of the mobility gap for a/nc-Si:H mixed-phase films. For low nc density, the Fermi energy resides in the middle of the gap, and only a fraction of the dangling bond states are occupied [shaded peak in Fig. 8(a)]. For X_C=0.02–0.04 [Fig. 8(b)], the embedded nanocrystals donate sufficient excess electrons to the surrounding a-Si:H matrix that the dangling bond band is fully occupied, shifting the Fermi energy closer to the conduction band edge. For higher nanocrystal concentrations [Fig. 8(c)], the number of additional dangling bonds increases faster than the excess charges donated by the nanocrystals, and the Fermi energy again resides in the middle of the gap.

then calculations suggest that the bandgap of the silicon nanoparticles is increased to about 1.4 eV, due to quantum confinement effect.[25,33] These same simulations suggest that if such a particle is surrounded by hydrogenated amorphous silicon, which has a mobility gap of 1.8 eV, then the conduction band edge of the nanocrystal is roughly 0.1 eV below that of the a-Si:H material, and the valence band of the nanoparticle is ~0.3 eV above the a-Si:H valence band edge.[37,38] It is well known that increasing the hydrogen content above ~10 at. % normally found in glow discharge deposited a-Si:H increases the optical gap of the amorphous semiconductor.[40] It is therefore reasonable that the hydrogen rich shell surrounding the silicon nanocrystal has a bandgap of approximately 2.0 eV. This is admittedly a rough estimate, but the exact value of the energy gap of the hydrogen rich shell surrounding the nanocrystal is not crucial for the argument below. For simplicity it is assumed that the energy band of the shell region is equally offset from the a-Si:H conduction and valence band edges.

At room temperature, there will be many electron-hole pairs thermally excited within the silicon nanocrystal. The electron experiences an energy barrier of approximately 0.2 eV from the a-Si:H conduction band edge, while the corresponding hole in the nanoparticle has a larger barrier of 0.4 eV inhibiting its motion into the a-Si:H valence band. It is thus reasonable that an electron thermally generated within the nanocrystal can escape to the surrounding a-Si:H film. The accompanying hole will remain trapped within the nanoparticle, leaving the nanocrystal positively charged. This positive charge inhibits additional electrons from escaping from the nanocrystal. We therefore propose that for every silicon nanocrystal embedded within the a-Si:H, one excess electron is donated to the surrounding material.

The photosensitivity measurements suggest that films deposited in the A and B locations have comparable dangling bond densities, while the films deposited in position C have higher, by roughly an order of magnitude, defect densities. These results are consistent with measurements of the spectral dependence of the optical absorption coefficient for the mixed-phase films, described in detail in a separate publication. The CPM results suggest that the films with the lowest nanocrystalline concentration (that is, those deposited at a location in the second plasma chamber at the greatest distance from the particle injection tube) have a dangling bond density of roughly 10^{17} cm^{-3}.[41] If the silicon nanocrystal has a diameter of ~5 nm, then it will be comprised of roughly 3300 Si atoms. A crystal fraction of 0.02 [corresponding to the films deposited at an intermediate distance from the particle injection tube, located at position B in Fig. 1(b)] then implies a density of 3×10^{17} cm^{-3} nanocrystals. If each nanocrystal donates an excess electron to the surrounding a-Si:H, then the density of excess negative charge introduced to the a/nc-Si:H film is also 3×10^{17} cm^{-3}. These excess charges will fall into the dangling bond defects in the middle of the energy gap of the a-Si:H. At a crystal fraction of 0.02, the density of donated charges is roughly comparable to the density of native dangling bond defects; consequently, all of the unoccupied dangling bonds (positively charged) will become singly occupied (neutral). The dark Fermi energy will thus be shifted up toward the conduction band edge and will reside in the minimum between the dangling bond band and the exponential conduction band tail states, as indicated in Fig. 8.

This enhancement in the dark conductivity by the excess charge donated by the nanocrystals is negated by the addition of defects when the nanocrystalline concentration is further increased. As indicated in the tm-AFM images (Fig. 2), films deposited on substrates located directly underneath the particle injection tube have a higher concentration of nanoparticle inclusions than would be expected by a simple extrapolation from the densities found in the substrates located at greater separations. Moreover, it is likely that films with high nanocrystal concentration contain more small nanocrystal agglomerates, which may form either in the gas phase or by

crystals depositing onto or next to other crystals that are already residing on the substrate. These agglomerates are more likely to lead to small voids due to shading effects during the amorphous film deposition. It is thus probable that a larger density of dangling bonds is associated with the higher nanoparticles densities in these films, consistent with the lower photosensitivity (Fig. 6 and Table I). Dangling bond defects act as recombination centers, and the higher their concentration, the lower the photoconductivity. When the crystal fraction is 0.10, the dangling bond density as determined by the midgap optical absorption coefficient is $\sim 3 \times 10^{18}$ cm^{-3}, compared to roughly 10^{17} cm^{-3} for the film with $X_c = 0.02$ crystal fraction.[40] However, if 10% of the mixed-phase material is crystalline, then with nanoparticles of diameter ~5 nm, this implies a density of nanocrystalline inclusions of $\sim 10^{18}$ cm^{-3}. Consequently, the excess charges donated by these inclusions would not be sufficient to maintain the dark Fermi level at its position closer to the conduction band edge [see Fig. 8(b)] and the dark conductivity activation energy will return to a value similar to that observed in films with less than $X_c < 0.01$ crystal fraction [see Fig. 8(c)].

In addition, the higher density of nanoparticles in the films deposited directly underneath the particle injection tube will likely increase the long range disorder at the mobility edges, resulting in the conduction band edge moving to higher energies, which would also tend to increase the dark conductivity activation energy and lower the conductance of these films.[29] Ideally one would compare the temperature dependence of the thermopower and dark conductivity to elucidate the role that increased long-range disorder by the nanocrystalline inclusions. However, the materials investigated here, which are undoped, are too resistive for accurate determinations of the thermopower. Experiments are underway to compare the conductivity and thermopower of phosphorus doped a/nc-Si:H films.

VII. SUMMARY

Mixed-phase thin films consisting of a hydrogenated amorphous silicon film in which silicon nanocrystals are embedded have been successfully synthesized in a dual-chamber codeposition system described here. By controlling the plasma conditions in one chamber, silicon nanocrystals of a given diameter are grown, which are then injected into a second chamber in which the a-Si:H is deposited. By varying the location of the deposition substrate relative to the outlet of the particle injection tube, one can fabricate several films with the silicon nanocrystal concentrations ranging from below 0.01 to above 0.10, in a single deposition run. In this way the role of increasing nanocrystal density can be accurately compared. Raman spectroscopy and tm-AFM measurements confirm that the nanocrystal density does indeed decrease as the substrate separation from the particle injection tube is increased.

At a moderate concentration (crystalline fraction $X_c \sim 0.02-0.04$) of silicon nanocrystallites, the dark conductivity is enhanced by up to several orders of magnitude compared to mixed-phase films with either lower or higher densities of nanoparticle inclusions. We propose that charges donated into the a-Si:H film by the nanocrystalline inclusions shift the Fermi energy closer to the conduction band edge, through the conversion of unoccupied dangling bond states to singly occupied, without an accompanying significant increase in defect density, increasing the dark conductivity of these films. Films containing much higher nanocrystalline concentrations also have higher dangling bond densities, which negate the doping effect of the nanocrystalline inclusions.

ACKNOWLEDGMENTS

This work was partially supported by the NSF under Grant Nos. NER-DMI-0403887 and DMR-0705675, the NINN Characterization Facility, the Xcel Energy grant under RDF Contract No. RD3-25, and the University of Minnesota Center of Nanostructure Applications. Lee Wienkes' assistance with optical absorption measurements and helpful comments from Paul Stradins and C. Blackwell are gratefully acknowledged. Y.A. and C.A. contributed equally to this work.

[1] P. R. Cabarrocas, S. Hamma, P. St'ahel, C. Longeaud, J. P. Kleider, R. Meaudre, and M. Meaudre, 14th European Photovoltaic Solar Energy Conference, Barcelona, Spain, 1997 (unpublished).
[2] J. Yang, K. Lord, S. Guha, and S. R. Ovshinsky, Mater. Res. Soc. Symp. Proc. **609**, A15.4.1 (2000).
[3] R. W. Collins, A. S. Ferlauto, G. M. Ferreira, J. Koh, C. Chen, R. J. Koval, J. M. Pearce, C. R. Wronski, M. Al-Jassim, and K. M. Jones, Mater. Res. Soc. Symp. Proc. **762**, A.10.1 (2003).
[4] C. R. Gorla, S. Liang, G. S. Tompa, W. E. Mayo, and Y. Lu, J. Vac. Sci. Technol. A **15**, 860 (1997).
[5] M. L. Ostraat, J. W. De Blauwe, M. L. Green, L. D. Bell, M. L. Brongersma, J. Casperson, R. C. Flagan, and H. A. Atwater, Appl. Phys. Lett. **79**, 433 (2001).
[6] T. C. Chang, S. T. Yan, P. T. Liu, C. W. Chen, Y. C. Wu, and S. M. Sze, Electrochem. Solid-State Lett. **7**, G13 (2004); Appl. Phys. Lett. **85**, 248 (2004).
[7] K. Nishiguchi, X. Zhao, and S. Oda, J. Appl. Phys. **92**, 2748 (2002).
[8] N.-M. Park, T.-S. Kim, and S.-J. Park, Appl. Phys. Lett. **78**, 2575 (2001).
[9] J. D. Joannopoulos, P. R. Villeneuve, and S. Fan, Nature (London) **386**, 143 (1997).
[10] G. Viera, S. Huet, M. Mikikian, and L. Boufendi, Thin Solid Films **403–404**, 467 (2002).
[11] G. Viera, M. Mikikian, E. Bertran, C. Roca, and L. Boufendi, J. Appl. Phys. **92**, 4684 (2002).
[12] M. Luysberg, C. Scholten, L. Houben, R. Carius, F. Finger, and O. Vetterl, Mater. Res. Soc. Symp. Proc. **664**, A15.2 (2001).
[13] S. Sriraman, S. Agarwal, E. S. Aydil, and D. Maroudas, Nature (London) **418**, 62 (2002).
[14] D. J. Lockwood, G. F. Grom, P. M. Fauchet, and L. Tsybeskov, J. Cryst. Growth **237–239**, 1898 (2002).
[15] Z. H. Lu, D. J. Lockwood, and J.-M. Baribeau, Nature **378**, 258 (1995).
[16] M. Fontcuberta i Morral, H. Hofmeister, and C. Roca, J. Non-Cryst. Solids **299–302**, 284 (2002).
[17] C. R. Wronski, J. M. Pearce, R. J. Koval, X. Niu, A. S. Ferlauto, J. Koh, and R. W. Collins, Mater. Res. Soc. Symp. Proc. **715**, 459 (2002).
[18] D. Staebler and C. Wronski, Appl. Phys. Lett. **31**, 292 (1977); J. Appl. Phys. **51**, 3262 (1980).
[19] L. Mangolini, E. Thimsen, and U. Kortshagen, Mater. Res. Soc. Symp. Proc. **862**, 307 (2005).
[20] S. D. Walck and J. P. McCaffrey, Thin Solid Films **308–309**, 399 (1997).
[21] C. Blackwell, C. Anderson, J. Deneen, C. Carter, U. Kortshagen, and J. Kakalios, Mater. Res. Soc. Symp. Proc. **910**, 79 (2006).
[22] S. Thompson, C. R. Perrey, C. B. Carter, T. J. Belich, J. Kakalios, and U. Kortshagen, J. Appl. Phys. **97**, 034310 (2005).
[23] G. Viera, S. Huet, and L. Boufendi, J. Appl. Phys. **90**, 4175 (2001).
[24] C. Min, Z. Weijia, W. Tianmin, J. Fei, L. Guohua, and D. Kun, Vacuum

81, 126 (2006).
[25]R. Saleh and N. H. Nickel, Thin Solid Films **427**, 266 (2003).
[26]G. Lucovsky, R. J. Nemanich, and J. C. Knights, Phys. Rev. B **19**, 2064 (1979).
[27]E. Bhattacharya and A. H. Mahan, Appl. Phys. Lett. **52**, 1587 (1988).
[28]Y. Lubianiker, J. D. Cohen, H. C. Jin, and J. R. Abelson, Phys. Rev. B **60**, 4434 (1999).
[29]D. Quicker and J. Kakalios, Phys. Rev. B **60**, 2449 (1999).
[30]D. B. Williams and C. B. Carter, *Transmission Electron Microscopy* (Plenum, New York, 1996).
[31]The crystalline silicon substrates used in run 1 were flawed and we were unable to obtain viable FTIR data for this run. As described in the text, the relative increase in infrared absorption at 2090 cm^{-1} with increasing nanocrystalline content is observed in all runs investigated, although there is some variance in the exact values of the microstructure factor R.
[32]D. C. Marra, E. A. Edelberg, R. L. Naone, and E. S. Aydil, J. Vac. Sci. Technol. A **16**, 3199 (1998).
[33]V. A. Burrows, Y. J. Chabal, G. S. Higashi, K. Raghavachari, and S. B. Christman, Appl. Phys. Lett. **53**, 998 (1988).
[34]M. Stutzmann, W. B. Jackson, and C. C. Tsai, Phys. Rev. B **32**, 23 (1985).
[35]P. Stradins, M. Kondo, and A. Matsuda, J. Non-Cryst. Solids **354**, 2144 (2008).
[36]P. Stradins, Sol. Energy Mater. Sol. Cells **78**, 349 (2003).
[37]A. H. Mahan and M. Vanecek, International Meeting on Stability of Amorphous Silicon Materials and Solar Cells, 1991 (unpublished), Vol. 234, p. 195.
[38]D. Kwon, J. D. Cohen, B. P. Nelson, and E. Iwaniczko, Mater. Res. Soc. Symp. Proc. **377**, 301 (1995).
[39]J. T. Stephen, D. Han, A. H. Mahan, and Y. Wu, Mater. Res. Soc. Symp. Proc. **420**, 485 (1996).
[40]J. M. Essick, Z. Nobel, Y.-M. Li, and M. S. Bennett, Phys. Rev. B **54**, 4885 (1996).
[41]L. Wienkes, *et al.* (unpublished).